Photovoltaic Responses In Ionically Self-Assembled Nanostructures Containing Conjugated Polymers And Fullerenes

C. Brands, T. Piok*, P. J. Neyman, A. Erlacher*, C. Soman, M. A. Murray,
R. Schroeder, J. R. Heflin, W. Graupner,
Department of Physics, Virginia Tech, Blacksburg, VA 24061-0435

D. Marciu, A. Drake, M. B. Miller,
Luna Innovations, Inc., P.O. Box 11704, Blacksburg, VA 24062-1704

H. Wang, H. Gibson, H. C. Dorn,
Department of Chemistry, Virginia Tech, Blacksburg, VA 24061-0212

G. Leising,
**Institut für Festkörperphysik, Technische Universität Graz, Graz, 8010 Austria*

M. Guzy, R.M. Davis,
Department of Chemical Engineering, Virginia Tech, Blacksburg, VA 24061-0211

ABSTRACT

We use the technique of ionically self-assembled monolayers (ISAMs) to produce photovoltaic devices of well-controlled thickness and composition. The ISAM nanostructure fabrication method simply involves the alternate dipping of a charged substrate into aqueous cationic and anionic solutions at room temperature. We have employed several approaches to combine the tetrahydrothiophenium precursor of poly(para-phenylene-vinylene) (PPV) with fullerenes and other organic materials. We apply modulation spectroscopy for the electro-optical characterization of the ISAM-devices. Analyzing the thickness dependence of the recorded photocurrent action spectra allows us to identify the photoactive region within the devices. The modulation frequency dependence of the photocurrent can be assigned to the influence of trapped charges taking part in the photovoltaic process. By utilizing the ability to control both thickness and composition of the organic layer at a nanometer level of precision, the composition and concentration of these defects has been systematically varied.

Keywords: photovoltaics, polyelectrolytes, ionically self-assembled monolayers, poly(para-phenylene-vinylene), fullerenes

1 INTRODUCTION

The ultrafast photoinduced electron transfer between conjugated molecules of appropriately chosen levels of the highest occupied molecular orbital (HOMO) and the lowest unoccupied molecular orbital (LUMO) has allowed the production of efficient organic photovoltaic devices.[1,2] Although there has been rapid progress in recent years, very fundamental questions of optical charge generation and transport in organic materials are not resolved yet which span fields from quantum mechanics to chemical engineering.[3,4,5,6] The absorption of light in a conjugated polymer primarily creates bound electron-hole pairs in their singlet state, singlet excitons (SE). It has become clear that the charge generation process in "pure" layers of conjugated molecules is driven by defects which serve as exciton dissociation centers.[7,8] In this sense, the incorporation of an electron accepting guest, such as the pure fullerene C_{60},[9] derivatized fullerenes[10] or others[11] in a poly(*para*-phenylene-vinylene) (PPV) host can be seen as an introduction of "defects". However, the main difference between defect-induced charge generation in pure PPV and the electron-donating-accepting process in PPV:C_{60} is that the electron remains on a PPV segment in the first case while in the latter it is transferred to the C_{60}. Since the exciton diffusion length in conjugated polymers is on the order of 10nm,[12] however, the charge generation can only occur if the dissociation site is within this distance of any given optically-excited electron-hole pair. It is the focus of this study to examine in detail the charge generation process in both pure and doped PPV.

Conjugated polymers offer the promise of easy fabrication of optoelectronic devices, especially when large area devices are considered. Changing the chemical composition of the conjugated polymer allows both tuning (1) the absolute values of the HOMO and LUMO levels as well as (2) the difference between the HOMO and the LUMO. Choosing a pair of two conjugated materials with the appropriate HOMO/LUMO levels ensures efficient charge generation[1] while the HOMO-LUMO difference is responsible for the matching of the spectral dependence of the sun's irradiance to the absorption of the photovoltaic element.

In *Micro- and Nano-photonic Materials and Devices*, Joseph W. Perry, Axel Scherer,
Editors, Proceedings of SPIE Vol. 3937 (2000) • 0277-786X/00/$15.00

Typically, the spin coating technique is used to produce layers of conjugated polymers. Alternate approaches are the doctor blade technique, which allows, for example, roll-to-roll processing or dip coating. A special variation of the dip coating approach produces exceptionally homogeneous thin films through the ionically self-assembled monolayer (ISAM) process. This method was developed by Decher and coworkers [13,14] and used for polymer light emitting diodes by Rubner and coworkers[15,16] as well as for nonlinear optical applications by us.[17] The ISAM method involves the alternate dipping of a charged substrate into an aqueous solution of a cation followed by dipping in an aqueous solution of an anion at room temperature (see Figure 1). Since the adsorption is based on the electrostatic attraction of interlayer charges, each layer is self-limiting in thickness and uniform at the molecular level. Sequential layers are rapidly fixed by drying at room temperature and ambient pressure. Multilayer films, up to several microns in thickness, are easily fabricated by repeating the dipping process with no limit to the number of layers that can be deposited. The resulting films are mechanically very robust.

It has been shown previously that the chemical nature of the fullerene acceptor,[18] the chemical composition of organic photodiodes[19] (e.g. molecular doping or heterolayer structures), and the film thickness[19] can strongly influence the photovoltaic efficiencies. We expect, therefore, to be able to optimize the performance of photovoltaic devices by varying the molecular components and the thickness of the respective layers at the nanometer scale. For this endeavor, the ISAM approach is the ideal route and we focus on a demonstration of its power.

The basic process that takes place in a solar cell can be described as follows: (1) light is absorbed and (2) produces charge carriers which have to (3) travel to collecting electrodes. For the first step, the high absorption coefficient and its anisotropy are natural advantages offered by conjugated organic molecules. However, it was shown that strong absorption does not necessarily coincide with a high probability for charge generation due to the different symmetries of the wavefunction of excited states.[3]

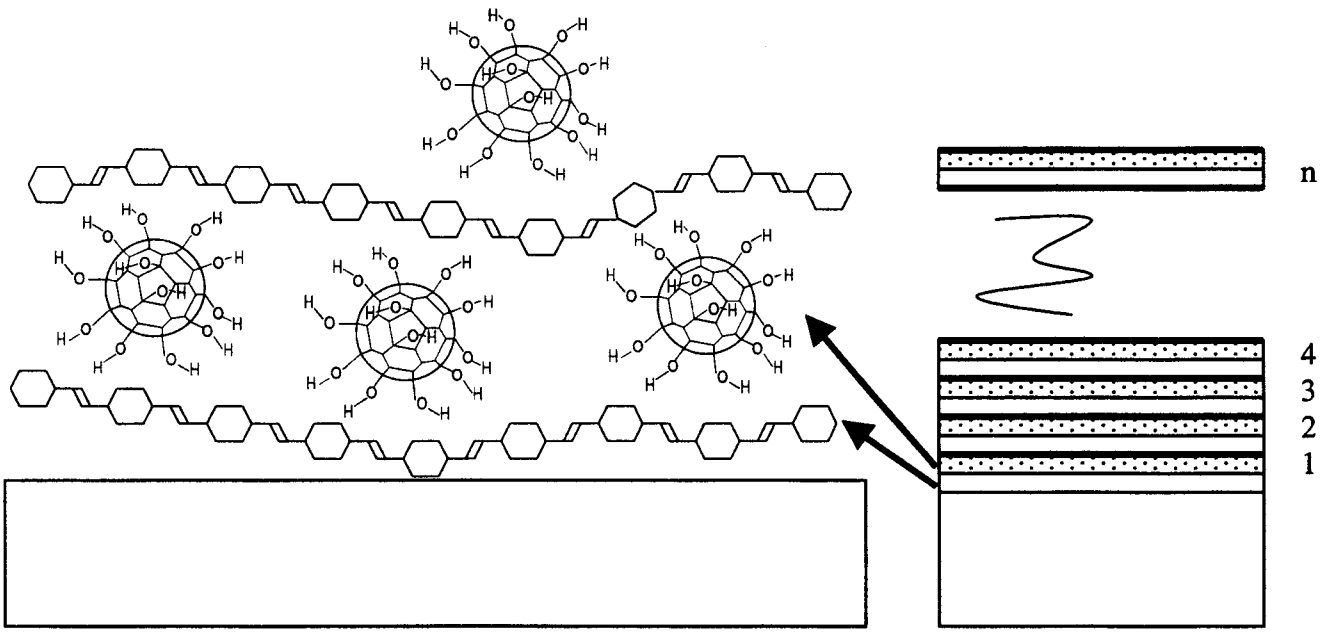

Figure 1: On the left we show the composition of the PPV- $C_{60}(OH)_{24}$ ISAM films on a molecular level. This is a "magnification" of the schematic bilayer structure on the right, which also explains the counting system in terms of bilayers. The grey area represents the substrate.

2 EXPERIMENTAL

2.1 Samples:

This Section describes the materials and parameters used for the ISAM devices. Since the variation of the concentration of the organic in the dipping solution, its pH value and its salt concentration strongly influence the monolayer formation process, we will give a detailed account in order to explain how we arrived at films of very different thickness and composition. In a related detailed study, the parameters of the dipping solutions for the absorbance of the films and thus, the thickness of the films were optimized.[20] Two basic variables have been studied that control the amount of PPV precursor adsorbed into each monolayer: the presence of salt in the PPVpc solutions, and the pH of the PPVpc solution. In general the ISAM layer structure is described by the scheme in Figure 1. In particular, we show a bilayer system based on PPV and

$C_{60}(OH)_{24}$. The data for the samples used in this study are compiled in Table 1. All optical and electrical measurements were performed in air at room temperature.

2.1.1 Chemistry

The basic constituents of the ISAM films in this study are PPV and poly(methacrylic acid) (PMA) as oppositely charged film forming agents. The conjugated PPV is insoluble – therefore we use its water-soluble cationic precursor version for the film production. This precursor is prepared via the classic route[21] and has already been used successfully for ISAM-based devices.[15] PMA was purchased from Polysciences. For an interface study, which was also conducted for light emitting diodes,[20] we used several polymers. The polythiophene acetic acid (PTAA) was prepared according to Ref. 22. Poly(allylamine hydrochloride) (PAH) and Cu-Phthalocyanine tetrasulfonic acid tetrasodium salt were purchased from Aldrich, and poly(sodium 4-styrenesulfonate) (PSS) was purchased from Polysciences. We have chosen $C_{60}(OH)_n$ as a water-soluble ionizable fullerene derivative which was purchased from MER Corporation in Tucson, AZ.When $C_{60}(OH)_n$ is synthesized, it yields a range of products which are not easily separated. The product we have used has an n-range of 22-26 for average composition of $C_{60}(OH)_{24}$. The pH and the ionic strength were adjusted as described below for the different studies. We will only report a selection of these parameters which are described comprehensively in Ref.20.

Table 1: Overview of a selection of the samples used in this investigation. The peak response describes the maximum photocurrent found for each of the 14 classes of devices we have investigated – so this has to be seen as the best value obtained and not a typical one since scattering from device to device is considerably large. Furthermore we want to note that the photocurrent action spectra are normalized to the incident intensity and not to the absorbed intensity. This means that we find the peak at around 330 nm since all photocurrent spectra showed a strong rise for decreasing wavelengths and the glass/ITO cuts off in this region. We have used the following terminology: $(A/B)_x$, where A, B denote the constituents of the bilayers and x denotes the number of bilayers.

Sample #	Sample Composition	Peak Response in [10^{-5}A/W]	Remarks
1	$(PPV/PMA)_{10}$	1	
2	$(PPV/PMA)_{20}$	4	
3	$(PPV/PMA)_{40}$	3.6	
4	$(PPV/PMA)_{32}$	90	Parameters for thick film
5	$(PPV/ C_{60}(OH)_{24})_{32}$	0.55	
6	$(PPV/ C_{60}(OH)_{24})_{32}$	32	Parameters for thick film
7	$(PAH/PT)_3(PPV/PMA)_{20}$	34	Parameters for thick film
8	$(PAH/PSS)_3(PPV/PMA)_{20}$	55	Parameters for thick film
9	$(PPV/PMA)_{20}$	19	Parameters for thick film
10	$(PPV/PMA)_{20}(PAH/PT)_{20}$	12	Parameters for thick film
11	$(PPV/PMA)_{20}(PAH/PSS)_3$	36	Parameters for thick film
12	$(PPV/CuPc)_{30}$	170	Parameters for thick film
13	$(PPV/CuPc/PPV/PMA)_{15}$	30	Parameters for thick film
14	$(PPV/PMA)_{30}$	20	Parameters for thick film

2.1.2 Film and Device Production

All films were prepared at room temperature and in air. The devices were built on glass substrates coated with indium tin oxide (ITO), provided by Delta Technologies. The glass substrate also had an antireflection coating on the side opposite to the ITO. For device production, regions of the ITO were etched off in order to get a structure which is depicted in Figure 2 (C). After the deposition of the films on glass slides and indium tin oxide (ITO) coated glass slides, the PPV films were converted at approx. 300°C for 8 hours in dynamic vacuum, using a liquid nitrogen cold trap. Evaporated aluminum was used as the top electrode of the devices. Typically we obtain 8 devices on a glass slide out of one production process.

We have employed two parameter sets for the film production – one optimized to obtain *thin films*, the other one optimized for obtaining *thicker films without having to go to very high numbers of bilayers.*

(i) **For the thin films** the concentrated PPV precursor solution (0.03 M) was diluted by a factor of 100 using a pH=3.7 of and 0.1 M concentration of the NaCl in the dipping solution.

(ii) **For the thick films** we increased the concentration of the PPV precursor dipping solution by a factor of ≈6 Also the pH was raised to 4.5 and the molarity of the NaCl to 0.3 M. The PMA dipping was done with 10 mM, pH=2.5, 0.1 M NaCl.

Pure PPV/PMA devices were produced in order to study the "pure" PPV response for varying thicknesses. We have investigated devices with 10, 20 and 40 bilayers (samples number 1,2,3 in Table 1) with the parameter-set used to obtain thin PPV films. However, we did also investigate thick PPV/PMA films, PPV/PMA films with several different interface structures and PPV/X-bilayers, where X represents an active species (for details see Table 1). The choice of PMA is based on the fact that it does not absorb above 300 nm, therefore we do not expect any active contribution to the optical properties of our devices which are limited by the ITO/glass absorption. Moreover it is known that the degree of interpenetration of the PPV films is high enough to sustain a good charge transport.

2.2 Photovoltaic Characterization

The spectral photovoltaic characterization was done with an Oriel 66002 light source, using a 150 W ozone free Xe lamp, operated at 104 W. The beam was passed through quartz lenses and an optical chopper and a CM 110 monochromator, equipped with a 2400 grooves/line grating, blazed at 250 nm. The area of the illuminated spot on the sample was 3 mm^2. Since the typical intensity across the range of 300 – 600 nm was 10 μW, the excitation density was on the order of 330 μW/ cm^2. The lamp intensity at the sample location was determined with an EG&G VACTEC CTB 100 photodiode. For the modulation measurements we used a chopper-frequency of 42 Hz. The photocurrent signal was picked up by a Standford Research System lock-in amplifier SR 830.

2.3 Optical Measurements

For the optical characterization, we have used a F20-UV thin-film measurement system by Filmetrics. The optical system consists of fiber mounts for reflection and transmission experiments as described in Figure 2 and its caption. Spectra are recorded by a fixed Czerny-Turner spectrometer with a 512-element photodiode array. As light sources, we used a regulated Tungsten Halogen lamp as well as a D-1000 Deuterium light source by OceanOptics.

The measurements yield two spectra:

(i) **the reflection spectrum R(λ)** – i.e. the fraction of light reflected by the complete layered structure.

(ii) **the transmission spectrum T(λ)** – i.e. the fraction of light transmitted through the complete layered structure.

These two spectra can be used to calculate

(iii) **the absorption spectrum A(λ)** - i.e. the fraction of light absorbed by the complete layered structure.

The calculation of A(λ) is based on the assumption that 1 = A(λ) + T(λ) + R(λ). It is important to note that this assumption even holds in the case of strong multiple beam interference as observed in our structures, however it fails in the case of strong scattering, as we show in Figure 4.

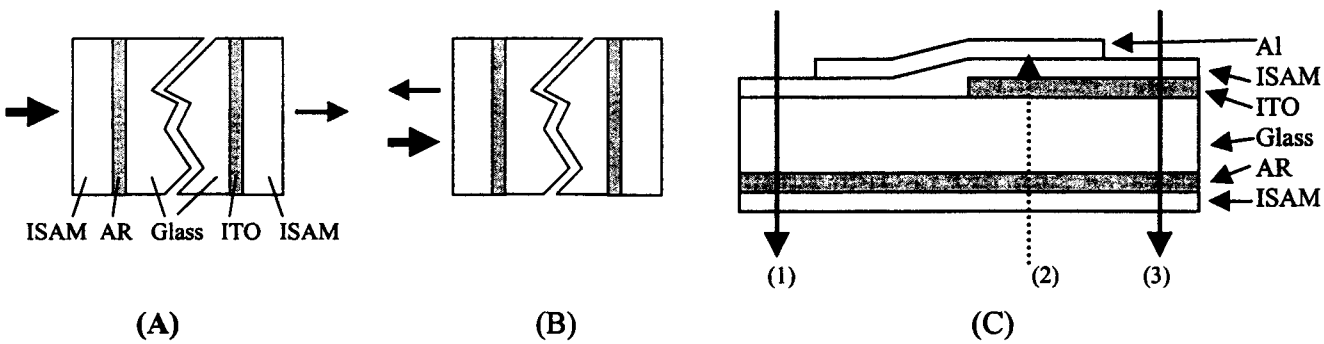

Figure 2: Principle of the complete optical characterization of the active layers of the devices in a region without Al, i.e. the electrode – see (C). The thick arrow denotes the incident light, the thin arrow denotes the transmitted light (A) or the reflected light (B). The abbreviations ISAM, AR, ITO refer to the organic layer, antireflection coating on the ITO and indium tin oxide. (C) explains, at which point of the device the optical characterization was performed. We have performed the measurements (A) and (B) in the glass/organic region [see arrows (1) and (3) in (C)], measurement (B) was also carried out in the region of the Al electrode (see arrow (2) in (C), for results see Figure 8).

3 RESULTS AND DISCUSSION

3.1 Photocurrent Action Spectra

We start this Section with the results obtained for pure PPV/PMA devices. Figure 3 shows the photocurrent action spectra as well as the optical spectra of the thin device layers (samples # 1-3 in Table 1) in the region where no Al is deposited. The

photocurrent response for these devices as well as the others is summarized in Table 1. The very low absolute values of the photocurrent response for all three samples can be understood easily when looking at the optical data. The very thin ISAM films do not show any signature of absorption by the PPV: We show this by plotting 1 - A (λ), which represents the transmitted intensity after correction for reflection. Obviously, the reflectivity clearly shows the presence of the very thin PPV film – the dips in the transmission spectra are primarily due to the peaks in the reflection, which are caused by the strong dispersion in the resonant region. Also, the photocurrent action spectra clearly show the onset for the PPV photocurrent at around 525 nm. The apparent peak in photovoltaic response at 330 nm is characteristic for the device and not for the PPV since we normalize our spectra with the incident radiation and not with the absorbed one. Therefore the strong decrease in photovoltaic response in these and all the following spectra represents the absorbance by glass and ITO. In order to obtain thicker films, we changed the film formation parameters as indicated in Section 2.1.2 – the results are shown in Figure 4.

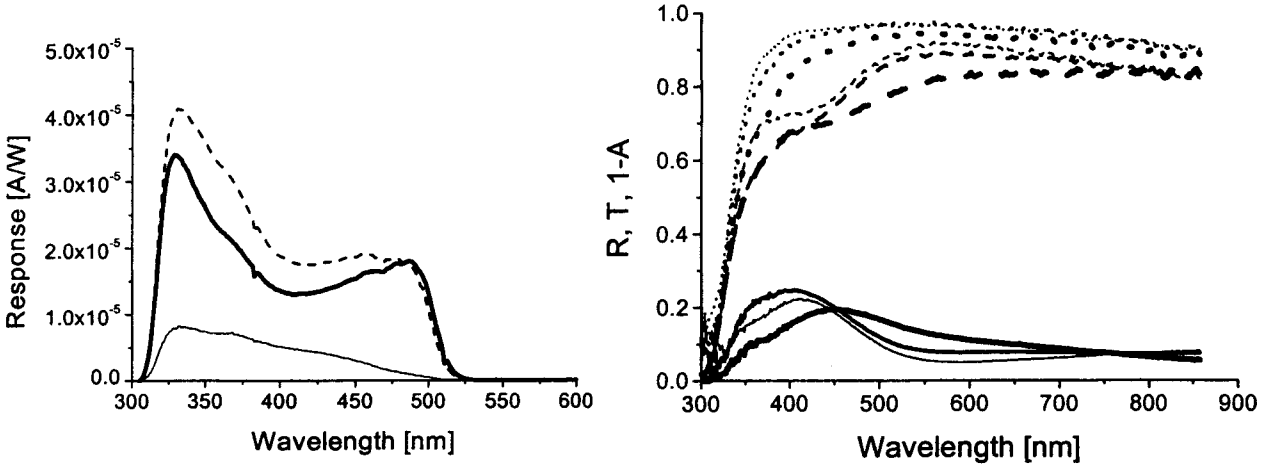

Figure 3: **Left:** photocurrent action spectra of the thin $(PPV/PMA)_n$ devices; thin line: n=10, dashed line: n=20, thick solid line: n=40. **Right:** measured reflection spectrum R(λ) – solid lines - and measured transmission spectrum T(λ) – dashed lines; calculated R(λ) + T(λ) – dotted lines. The latter corresponds to 1 - A (λ). The different line thickness denotes the three devices: thin line: n=10, medium line: n=20, thick line: n=40.

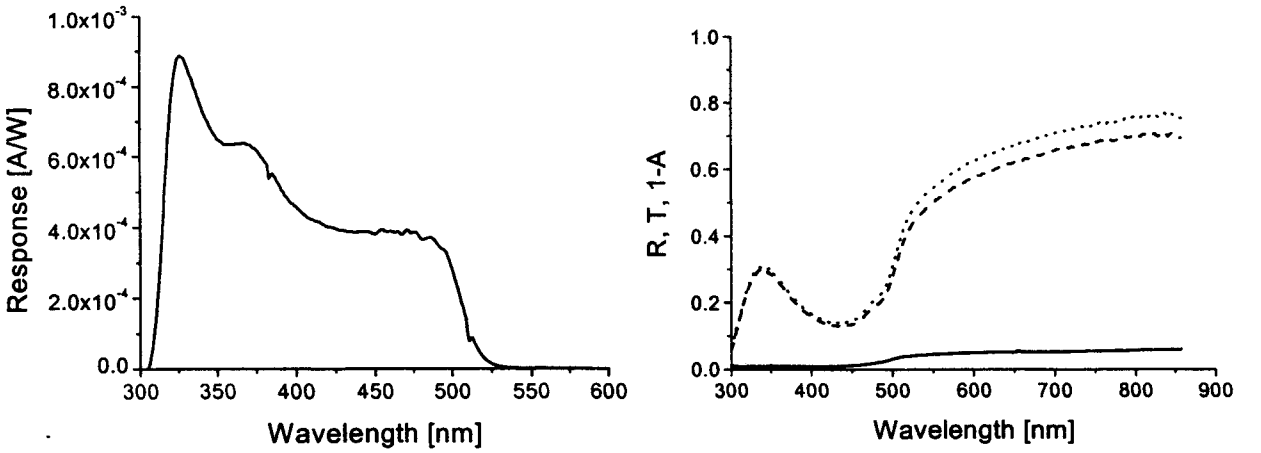

Figure 4: **Left:** photocurrent action spectra of the thick $(PPV/PMA)_{32}$ devices. **Right:** measured R(λ) (solid line) and and T(λ) (dashed lines), calculated R(λ) + T(λ) = 1- A (λ) (dotted line).

The photovoltaic response of the thick PPV film is more than an order of magnitude higher than the response observed for the very thin films, which were barely detectable in the absorption spectra. In contrast, the thick PPV film can be clearly in the right part of Figure 4. We want to add that the apparent absorption above 500 nm is due to strong scattering of light in this particular device. This scattering process also obscures the reflection spectra. We have not observed similar effects for other films.

In order to investigate the influence of the inclusion of $C_{60}(OH)_{24}$ on the photovoltaic response of the devices, we have investigated thin PPV/$C_{60}(OH)_{24}$ devices. As can be seen from Figure 5, the photocurrent action spectrum changes completely as compared to PPV: there is no clear onset at 525 nm as observed for the PPV in Figure 3 and Figure 4 as well as in samples number 7 – 14 of Table 1. The optical spectra in Figure 5 basically confirm the measurements we have obtained for the thin PPV layers: the presence of organic films can merely be deduced from the reflection spectra. Moreover we can conclude that the inclusion of the $C_{60}(OH)_{24}$ in the film forming process seems to suppress any signatures of the PPV in both the optical as well as the optoelectronic characterization.

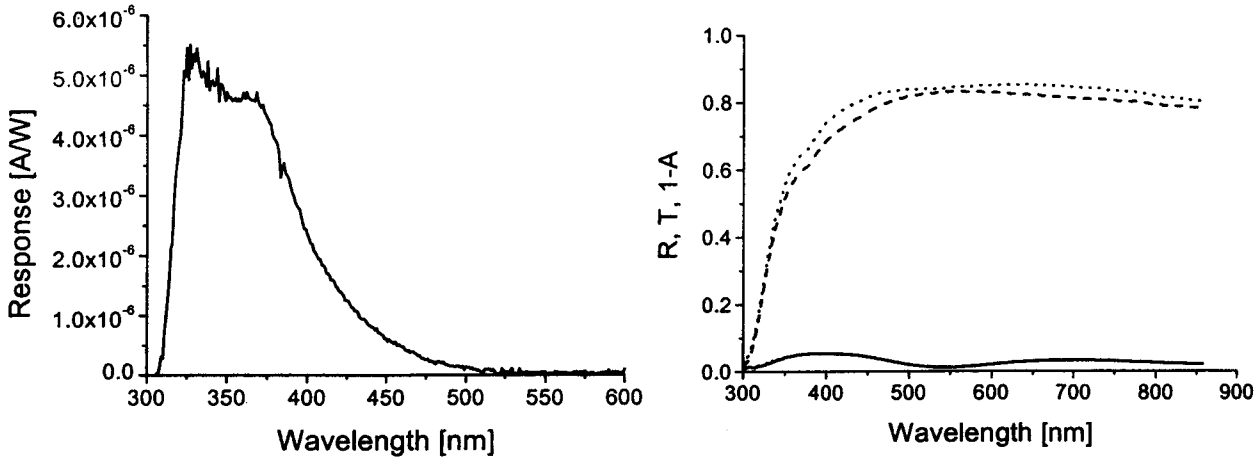

Figure 5: **Left:** photocurrent action spectra of the thin PPV/$C_{60}(OH)_{24}$ devices. **Right:** measured R(λ) (solid line) and and T(λ) (dashed lines), calculated R(λ) + T(λ) = 1- A (λ) (dotted line).

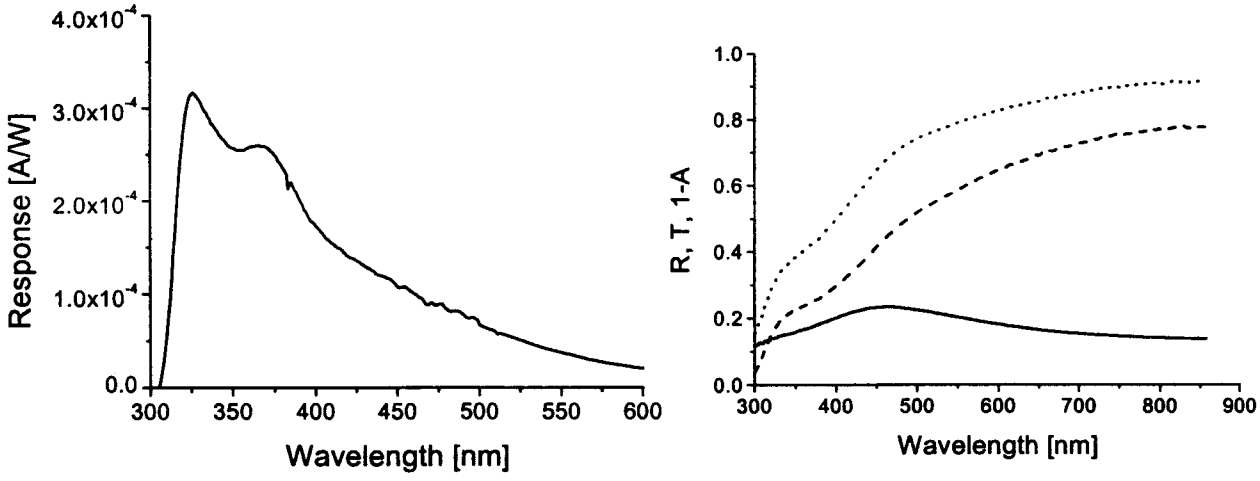

Figure 6: **Left:** photocurrent action spectra of the thick $(PPV/C_{60}(OH)_{24})_{32}$ devices. **Right:** measured R(λ) (solid line) and T(λ) (dashed line), calculated R(λ) + T(λ) = 1- A (λ) (dotted line).

The suppression of the observed electrical and optical PPV signatures is also observed in a thick sample, consisting of 32 bilayers of (PPV/$C_{60}(OH)_{24}$) as shown in Figure 6. In addition, also the time-constants observed in these devices are completely different from what is observed for the thick $(PPV/PMA)_{32}$ devices. This behavior is described in detail in Section 3.3. The conclusion from these experiments is that the $(PPV/C_{60}(OH)_{24})_n$ devices contain relatively low amounts of PPV. Therefore we are observing the photovoltaic properties of $C_{60}(OH)_{24}$. In order to overcome this shortcoming, $(PPV/PMA/PPV/C_{60}(OH)_{24})_n$ devices are being produced. However, there are also other potential molecular dopants which are expected to increase the photovoltaic response. We have decided to use Cu-Phthalocyanine tetrasulfonic acid tetrasodium salt (CuPc) and report the results in Figure 7.

The inclusion of CuPc into the production process of thick PPV films at two levels of concentration results in a clear improvement of the photocurrent response as we use a higher CuPc concentration and does not inhibit the PPV deposition as observed for the inclusion of $C_{60}(OH)_{24}$. The optical spectra in Figure 7 confirm all the assumptions made about the film production process. The PPV is clearly visible both in the reflection spectra at around 500 nm (compare also Figure 3 and Figure 8) and with the absorption peaking at about 400 nm. The absorption peak at 690 nm stems from CuPc and confirms its presence in the film. The strength also scales with the CuPc concentration, supporting the expected 2:1 ratio for the CuPc concentration in the $(PPV/CuPc)_{30}$ and $(PPV/CuPc/PPV/PMA)_{15}$ devices.

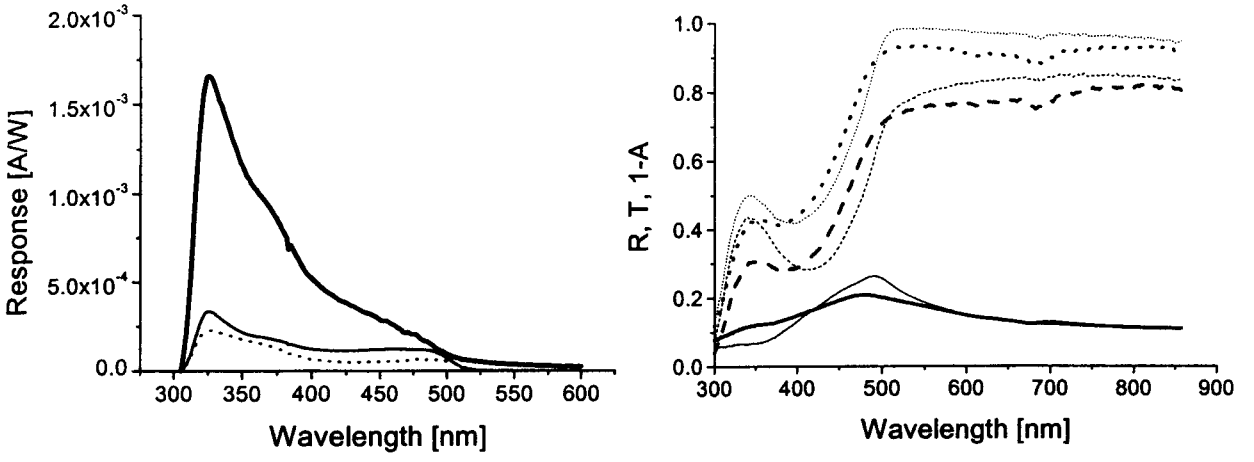

Figure 7: **Left:** photocurrent action spectra of $(PPV/CuPc)_{30}$ (thick line) and $(PPV/CuPc/PPV/PMA)_{15}$ (thin line). The dotted line shows the response of a $(PPV/PMA)_{30}$ for comparison. **Right:** measured R(λ) (solid lines) and T(λ) (dashed lines), calculated R(λ) + T(λ) = 1- A (λ) (dotted lines). The thick and thin lines refer to $(PPV/CuPc)_{30}$ and $(PPV/CuPc/PPV/PMA)_{15}$ respectively.

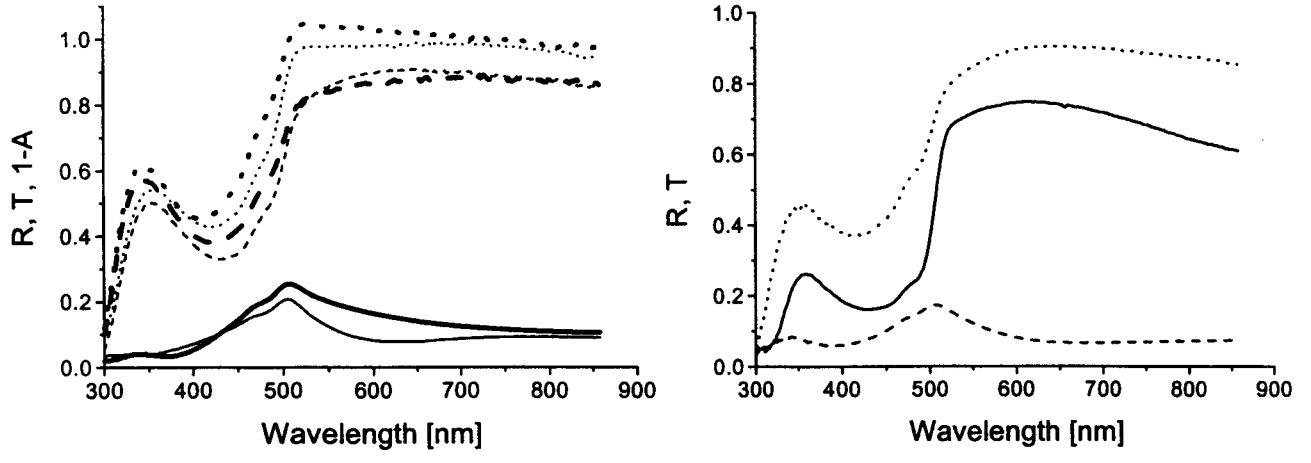

Figure 8: **Left:** measured R(λ) (solid lines) and T(λ) (dashed lines), calculated R(λ) + T(λ) = 1- A (λ) (dotted lines). The thick lines show the result for the layers without ITO, the thin lines represent the layers with ITO. Device: $(PPV/PMA)_{20}(PAH/PSS)_3$. **Right:** reflection without Al-electrode (dashed) and with Al-electrode (solid) as well as transmission without Al-electrode (dotted) for a $(PPV/PMA)_{20}(PAH/PT)_{20}$-device. For the measurement scheme see Figure 2.

3.2 Optical Properties

In the previous Section, we have shown the optical spectra corresponding to the various devices. All of these spectra were taken in a region with ITO and without aluminum (see Figure 2). However, we also want to show how the ITO layer as well as the Al layer influences the optical properties. Therefore we have first investigated one device both in a region of

glass/ITO/organic-film and of glass/organic film (for the scheme see Figure 2, results see Figure 8 left). The results show that the ITO hardly influences the fractions of reflected, transmitted and absorbed light in the device layers. In order to quantify how the Al-electrode influences the optical device properties we have done reflection measurements through the glass in a region of the Al-electrode and compare it to the reflection of the active layer system without Al (Figure 8 right). It is clear the reflection becomes very high through the Al electrode – however, the amount of light absorbed by the PPV is also substantially increased, since the light passes though the diode twice. In general, these spectra are in excellent agreement with a simple theoretical description by a Kramers-Heisenberg dielectric function, which is also called Helmholtz-Ketteler dielectric function or Lorentz oscillator. The peak in reflectivity, corresponding to the change in the real part of the dielectric function at around 500 nm, is due to the π-electron system of PPV. This π-electron system also causes the absorption peak at around 410 nm. In agreement with the Kramers-Heisenberg formalism, the transmission curve is therefore a superposition of the contributions of reflection and transmission, leading to a shift between the observed transmission peak and the true absorption peak. This emphasizes that neglecting reflection in determining the absorption from a transmission spectrum leads to considerable errors in the peak position, especially for thin films.

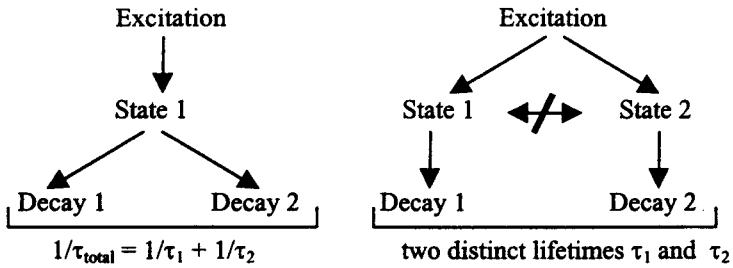

Figure 9: This Figure shows how a process that involves the creation of excited states and their decay via two processes leads to *one effective lifetime* (left). If there is an initial branching in two different kinds of uncoupled excited states (right) with two different decay processes, *both decay times* are observed.

3.3 Photocurrent Action Spectra – Phase and Frequency.

As described in the experimental Section 2.2, we have used a phase-sensitive modulation technique (lock-in amplifier) for the optoelectronic characterization of the devices. In general, every experiment of this kind yields two results – a signal intensity and a phase shift. We will start this discussion by describing how time constants, inherent to the probed system, influence the modulation results. The influence of a time-constant or lifetime τ on the signal vector $\vec{R}$ measured in a typical modulation experiment with a lock in amplifier can be described in the following manner:

$$\vec{R} = \frac{\vec{c}\left\{\exp\left[i\tan^{-1}(2\pi f\tau)\right]\right\}}{\sqrt{1+(2\pi f\tau)^2}} \qquad \text{Equation 1}$$

if a single time-constant or lifetime is involved. The previous result is the same as obtained for a simple low pass filter. If two time-constants are involved, the two processes lead to a signal vector, which is the sum of the two signal vectors that would be observed if one of the two processes was be "turned of":

$$\vec{R} = \frac{\vec{c}_1\left\{\exp\left[i\tan^{-1}(2\pi f\tau_1)\right]\right\}}{\sqrt{1+(2\pi f\tau_1)^2}} + \frac{\vec{c}_2\left\{\exp\left[i\tan^{-1}(2\pi f\tau_2)\right]\right\}}{\sqrt{1+(2\pi f\tau_2)^2}} \qquad \text{Equation 2}$$

where $\vec{R}$ is the intensity of the signal, f is the modulation frequency, τ, τ_1 and τ_2 are the lifetimes of the involved species or time-constants, as introduced to diodes via their depletion layer capacitance. Furthermore, $\vec{c}$, $\vec{c}_1$ and $\vec{c}_2$ represent the weight of each component. $\vec{R}$ has to be written in vector form since it describes both the intensity and the phase of the signal relative to the excitation, i.e. in our case the modulated beam of the Xe-lamp. If there are two time-constants involved, it means that there is an initial branching in the population into two separate *uncoupled* states, which decay with different decay rates. If the decay takes place from the same state, the decay rates will just add up to $k_{total} = k_1 + k_2$ with the "lifetime" to be $1/\tau_{total} = 1/\tau_1 + 1/\tau_2$. The physical meaning is that there is no single state with one lifetime but there are uncoupled states with different lifetimes. With respect to optoelectronic device characterization, one has to emphasize that a lifetime of the charge carriers (τ_1) and a device time-constant, caused by the capacitance and resistance ($RC=\tau_2$), would exactly add up in the described way of $1/\tau_{total} = 1/\tau_1 + 1/\tau_2$.

If we look at the two-dimensional vector described in Equation 2 we can either express the x and the y component or the radius (=intensity I) and the phase angle θ, with c being the intensity at f=0:

$$I = \frac{c}{\sqrt{1+(2\pi f\tau)^2}} \qquad \text{Equation 3}$$

$$\theta = \tan^{-1}(2\pi f\tau) \qquad \text{Equation 4}$$

If the experimental situation has to be described by two decay-times, one has to evaluate Equation 2 in order to express intensity and phase angle. However, if the second decay-time τ_2 is very small compared to the largest value used for the inverse modulation frequency, we can set τ_2 equal to zero (see modeling in Figure 10 and Figure 11, Table 2). The τ_2-related process does not influence the phase of the signal, i.e. Equation 4 remains valid. Equation 3 has to be modified for this case in order to add the frequency-independent part of the intensity c_2:

$$I = \frac{c_1}{\sqrt{1+(2\pi f\tau_1)^2}} + c_2 \qquad \text{Equation 5}$$

Before we show how these equations perfectly describe the experimental behaviour, we want to emphasize the physical interpretation of this formalism:

(i) The number of decay-times and their values found in the photocurrent modulation experiments express the number of different states and their contribution to the process of charge transport in the photovoltaic devices.

(ii) Modeling the recorded $I(f)$ curves allows us to retrieve a very important additional piece of information: the quasi-steady value of the photocurrent which can be obtained by extrapolating to f=0.

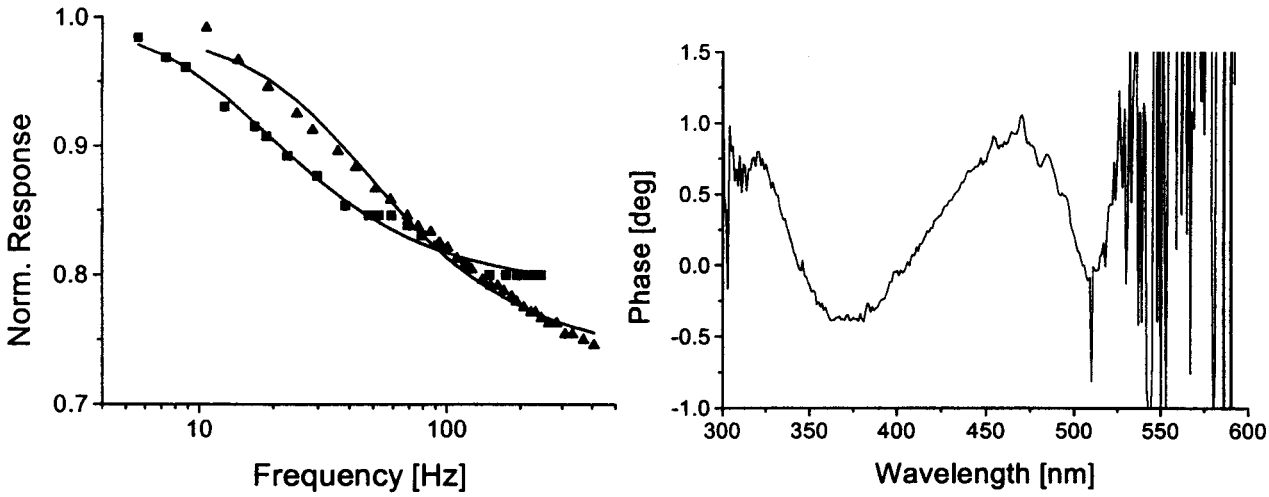

Figure 10: **Left:** normalized photocurrent vs. chopper frequency for the thick $(PPV/PMA)_{32}$ devices. Triangles denote the results obtained for the excitation wavelength λ_{exc}=500 nm, squares refer to λ_{exc}=350 nm. **Right:** Phase angle of the spectrally resolved photocurrent as displayed in Figure 4. The noise above 520 nm is due to the fact that the device has the onset for the photocurrent at about this value.

In the left part of Figure 10, we show the dependence of the photocurrent on the chopper frequency at excitation wavelengths λ_{exc} of 350 nm and 500 nm for the thick $(PPV/PMA)_{32}$ devices. These curves can readily be modeled with Equation 5 – the results are shown in Table 1. We see that at λ_{exc} = 500 nm the frequency-independent part – associated with the time-constant τ_2 = 0s – is slightly weaker than at 350 nm (weight of 0.75 vs. 0.80). Furthermore, the time-constant of the frequency dependent part is 4.9 ms at 500 nm as compared to 12 ms at 350 nm. The frequency-dependent measurement was only done for two wavelengths – however, the phase spectrum, which is measured as we record the photocurrent action spectra, contains similar information – though not as detailed. If one compares the phase angles recorded at 350 and 500 nm, it

becomes clear that both are rather small but that the value at 350 nm is larger, therefore leading to a larger time constant, following Equation 4. In order to confirm that this interpretation is correct, we have tried several other devices.

The thin PPV devices did not show any frequency dependence of the photocurrent for chopper frequencies between 4 and 400 Hz, in accordance to its very small phase angle. We will therefore present the results for devices which showed a large phase angle of the photocurrent: the thick $(PPV/C_{60}(OH)_{24})_{32}$ devices – see Figure 11 right. In accordance with the phase angles detected at 350, 500 and 580 nm, we have confirmed by frequency-dependent measurements (Figure 11 left), that the weakest frequency dependence is observed at 580 nm (smallest phase angle of about 2^{O}) and the strongest frequency dependence is observed at 350 nm (largest phase angle of about 10^{O}). Furthermore, comparing the data in Figure 10 and Figure 11 also shows clearly that the two materials behave very different under identical excitation conditions. This is further support for the hypothesis that the constituents of these devices are very different.

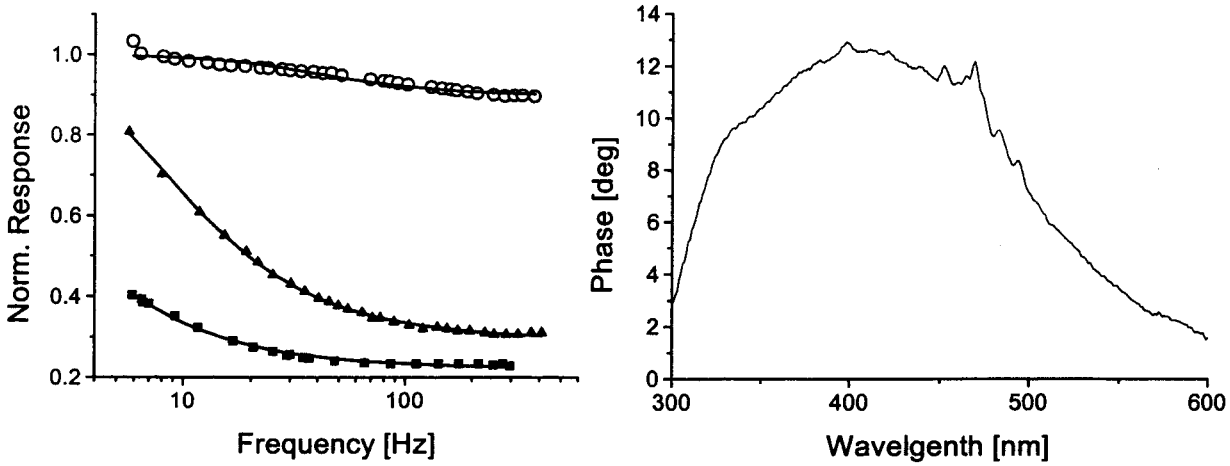

Figure 11: **Left:** normalized photocurrent vs. chopper frequency for the thick $(PPV/C_{60}(OH)_{24})_{32}$ devices. Open circles denote the results obtained for the excitation wavelength λ_{exc}=580 nm, triangles refer to λ_{exc}=500 nm, squares refer to λ_{exc}=350 nm. **Right:** Phase angle of the spectrally resolved photocurrent as displayed in Figure 6. The noise above 520 nm is due to the fact that the device has the onset for the photocurrent at about this value.

Table 2: A selection of parameters extracted from the analyses of the frequency dependent data in Figure 10 and Figure 11. The modeling is based on Equation 5. The weights c_1 and c_2 have been normalized, so that $c_1+c_2=1$.

Device	$\lambda_{exc.}$	c_1	τ_1 [ms]	c_2	τ_2 [ms]
$(PPV/PMA)_{40}$ – thin	500			1	0
$(PPV/PMA)_{32}$-thick	350	0.20	12	0.80	0
$(PPV/PMA)_{32}$-thick	500	0.25	4.9	0.75	0
$(PPV/C_{60}(OH)_{24})_{32}$-thick	350	0.78	110	0.22	0
$(PPV/C_{60}(OH)_{24})_{32}$-thick	500	0.71	27	0.29	0
$(PPV/C_{60}(OH)_{24})_{32}$-thick	580	0.10	6	0.90	0

3.4 Photocurrent Action Spectra – Radius Information

The charge generation process at wavelength λ in organic photovoltaic cells can be modeled by assuming an exponentially decaying *spatial and spectral energy density* in $J/(nm^2)$ in the layer of depth x – the decay is determined by the absorption coefficient $\alpha(\lambda)$ via Lambert-Beer's law:

$$e = e_o(\lambda)\exp[-\alpha(\lambda)x] \qquad \text{Equation 6}$$

The constant e_0 can be found by a proper normalization which ensures that the *spectral energy density* [J/nm] impinging on the film is the same (=E) for all wavelengths (=correction for constant power of illumination) :

$$E = \int_{x=0}^{\infty} e_o(\lambda)\exp[-\alpha(\lambda)x]dx \Rightarrow E = [-e_o(\lambda)/\alpha(\lambda)]\exp[-\alpha(\lambda)x]\Big|_0^{\infty} \Rightarrow$$

Equation 7

$$E = const. = e_o(\lambda)/\alpha(\lambda) \Rightarrow e_o(\lambda) = E * \alpha(\lambda)$$

Neglecting reflection, the absorbed energy-density can then be expressed for a finite thickness d:

$$E_{abs} = \int_{x=0}^{d} E * \alpha(\lambda)\exp[-\alpha(\lambda)x]dx = -E\exp[-\alpha(\lambda)x]\Big|_0^{d}$$

Equation 8

$$E_{abs} = E\{1-\exp[-\alpha(\lambda)d]\}$$

In the low excitation density limit, excluding any bimolecular decay processes, the photocurrent (PC) is proportional to the absorbed energy if we can assume that the generation efficiency is independent of the wavelength of the excited light. Especially the latter assumption is a very problematic one as we know from action spectra for charge generation, measured optically[23]. In the limit of very thin films, we obtain that the wavelength dependence of the photocurrent follows the absorption coefficient:

$$PC \propto E_{abs} = E\{1-1+\alpha(\lambda)d-...\}$$

$$PC \propto \alpha(\lambda)d$$

Equation 9

For thick films we obtain saturation, i.e a plateau-like behavior in the absorbing region:

$$PC \propto E_{abs} = E = const.$$

Equation 10

However, in most photodetectors light is absorbed in regions where it cannot contribute to charge generation since these regions are too far away from the active zone. This wavelength-dependent effect can be described by introducing an inactive layer of thickness $d_{inactive}$ through which the light passes like through an internal filter. For our devices, this internal filter is glass, ITO and even the organic layer itself. After passing this layer, light will hit the active zone of thickness d_{active}. Including the reflectivity to account for light which never enters the device or reaches the active region we get:

$$PC(active+inactive layer) \propto (1-R)(1-E_{abs,inactive})*(E_{abs,active}) =$$

$$(1-R)(1-\{1-\exp[-\alpha(\lambda)d_{inactive}]\})*(1-\exp[-\alpha(\lambda)d_{active}]) =$$

$$(1-R)(\exp[-\alpha(\lambda)d_{inactive}])*(1-\exp[-\alpha(\lambda)d_{active}])$$

Equation 11

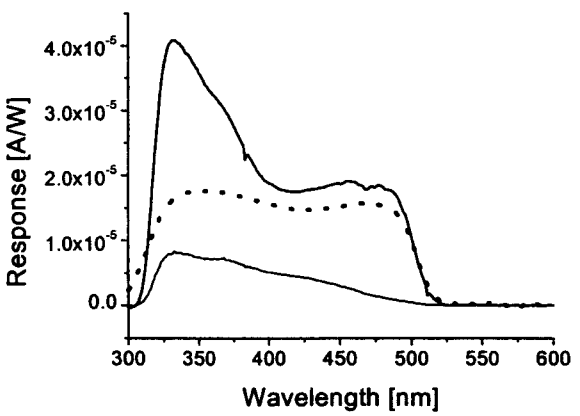

Figure 12: Modeling of the spectral response of a photovoltaic cell as shown in Figure 3 (experimental: thin line – 10 bilayers, thick line – 20 bilayers; dotted line – model based on Equation 11).

The behavior resulting from the previous equations is shown in Figure 12. The spectral response of the photocurrent could not be described properly in the region of small wavelengths. This result was also found for all the other devices we tried to model. This suggests that neglecting the fact that the charge generation efficiency increases with decreasing wavelength[23] (assumption to derive Equation 9) might be responsible for this problem. Moreover we do not take multiple beam interference into account.[24]

CONCLUSIONS

In summary, we have shown how the ISAM technique can be used to control the molecular composition of organic optoelectronic devices on the nanometer level. We have described how to produce thin and thick ISAM films with a comparable amount of bilayers. We have quantitatively discussed the influence of thickness and incorporating other materials into the ISAM layers. Moreover, we have given a detailed description of the optical properties of the devices. Finally, we have shown how the time constants influence the photovoltaic process.

ACKNOWLEDGEMENTS

Acknowledgement: This work has been partly supported by Air Force SBIR F49620-98-C-0074 and NSF Science and Technology Center DMR 9120004. A.E. acknowledges Landesregierung Kärnten. The Virginia Tech Aspires program and the Austrian Ministry for Science supported A.E. and T.P.

REFERENCES

[1] C. W. Tang, *Appl. Phys. Lett.* **48**, pp. 183-185 (1986).
[2] M. Granstrom, K. Petritsch, A. C. Arias, A. Lux, M. R. Andersson, R. H. Friend, *Nature* **395**, 257 (1998).
[3] A. Köhler, D. A. dos Santos, D. Beljonne, Z. Shuai, J.-L. Bredas, A. B. Holmes, A. Kraus, K. Müllen, R. H. Friend, *Nature* **392**, 903-906 (1998).
[4] D. Moses, J. Wang, G. Yu, A. J. Heeger, *Phys. Rev. Lett.* **80**, 2685 (1998).
[5] W. Graupner, G. Cerullo, M. Nisoli, G. Lanzani, E. J. W. List, G. Leising, S. De Silvestri, *Phys. Rev. Lett.* **81**, 3259-3262 (1998).
[6] V. I. Arkhipov, E. V. Emelianova, H. Bässler, *Phys. Rev. Lett.* **82**, 1321 (1999).
[7] E. Frankevich, A. Zakhidov, K. Yoshino, Y. Maruyama, K. Yakushi, *Phys. Rev. B* **53**, (1996).
[8] B. Dulieu, J. Wéry, S. Lefrant, J. Bullot, *Phys. Rev. B* **57**, 9118 (1998).
[9] N. S. Sariciftci, D. Braun, C. Zhang, V. I. Srdanov, A. J. Heeger, G. Stucky, F. Wudl, *Appl. Phys. Lett.* **62**, 585-587 (1993).
[10] G Yu, A. J. Heeger, *J. Appl. Phys.* **78**, 4510-4515 (1995); G Yu, J Gao, J C Hummelen, F Wudl, A. J. Heeger, *Science* **270**, 1789-1791 (1995); J. J. M. Halls, C. A. Walsh, N. C. Greenham, E. A. Marseglia, R. H. Friend, S. C. Moratti, A. B. Holmes, *Nature* **376**, 498-500 (1995).
[11] A. C. Arango, S. A. Carter, P. J. Brock, *Appl. Phys. Lett.* **74**, pp. 1698-1700 (1999).
[12] A. Haugeneder, M. Neges, C. Kallinger, W. Spirkl, U. Lemmer, J. Feldmann, U. Scherf, E. Harth, A. Gügel, K. Müllen, *Physical Review B* **59**, 15346 (1999).
[13] G. Decher and J. D. Hong, *Makromol. Chem., Makromol. Chem. Symp.*, **46**, 321 (1991).
[14] G. Decher, J. D. Hong, and J. Schimitt, *Thin Solid Films*, **210/211**, 831 (1992).
[15] A. C. Fou, O. Onitsuka, M. Ferreira, M. F. Rubner, and B. R. Hsieh, *J. Appl. Phys*, **79**, 7501 (1996).
[16] J-K. Lee, D. Yoo, and M. F. Rubner, *Chem. of Materials*, **9**, 1710 (1997).
[17] J.R. Heflin, C. Figura, D. Marciu, Y. Liu, and R.O. Claus, Appl. Phys. Lett. 74, 495 (1999); K.M. Lenahan, Y. Wang, Y. Liu, R.O. Claus, J.R. Heflin, D. Marciu, and C. Figura, Adv. Mater. 10, 853 (1998); J. R. Heflin, Y. Liu, C. Figura, D. Marciu, R. O. Claus, *Proc. SPIE*, **3147**, 10 (1997).
[18] C. Waldauf, W. Graupner, S. Tasch, G. Leising, U. Scherf, K. Müllen, *Optical Materials* **9**, 449-453 (1998).
[19] G. Meinhardt, W. Graupner, G. Feistritzer, R. Schroeder, E.J.W. List, A. Pogantsch, G. Dicker, B. Schlicke, A. D. Schlüter, G. Winter, M. Hanack, U. Scherf, K. Müllen, G. Leising, *SPIE Proceedings* **3623**, 46-57 (1999).
[20] D. Marciu, M. Miller, A.L. Ritter, M.A. Murray, P.J. Neyman, W. Graupner, J.R. Heflin, H. Wang, H.W. Gibson, R.M. Davis, *SPIE Proceedings* **3938** *in print.*
[21] F. R. Denton III, P. M. Lahti, F. E. Karasz, *J. Polym. Sci. Part A: Polym. Chem.*, **30**, 2223 (1992).
[22] A. T. Royappa, M. F. Rubner, *Langmuir* **1992**, *8*, 3169.
[23] V. I. Arkhipov, E. V. Emelianova, H. Bässler, *Phys. Rev. Lett.* **82**, 1321 (1999). M. Wohlgenannt, W. Graupner, G. Leising, Z. Vardeny, *Physical Review Letters* **82**, 3344-3347 (1999); M. Wohlgenannt, W. Graupner, G. Leising, Z. Vardeny, *Physical Review B* **60**, 5321-5330 (1999) and references therein.
[24] Leif A. A. Pettersson, Lucimara S. Roman, Olle Inganäs, *J. Appl. Phys.* **86**, pp. 487-496 (1999).